DNA Protonuclei as Programmable Nuclear Mimics Reveal Environmental Context on Protein Phase Separation

Johann Fritzen[1], Avik Samanta[2], Nele S. Kuhr[3], Erin L. Sternburg[3], Dorothee Dormann[3,4]*, Andreas Walther[1,5]*

[1] Life-Like Materials and Systems, Johannes Gutenberg University, 55128 Mainz, Germany
[2] Indian Institute of Technology Kharagpur, West Bengal, India
[3] Institute of Molecular Physiology, Johannes Gutenberg University, 55128 Mainz, Germany
[4] Institute of Molecular Biology (IMB), 55128 Mainz, Germany
[5] Max Planck Institute for Polymer Research, 55128 Mainz, Germany.
*Corresponding author. Email: andreas.walther@uni-mainz.de; ddormann@uni-mainz.de

Summary

Understanding protein phase separation in cellular environments remains a major challenge, as *ex vivo* assays often fail to capture the influence of environmental context – such as crowding, multimodal interactions, and the dynamic properties of the cytosol or nucleus. Here, we introduce programmable DNA-based protonuclei (PN) as nucleus-mimicking compartments to probe phase separation of the neurodegeneration-linked protein FUS. We show that FUS partitioning and condensate formation are highly sensitive to nucleic acid sequence, spatial confinement, and viscoelastic properties of the PN core. Notably, classical test-tube affinity assays fail to predict protein behavior within the crowded and multivalent PN environment. By tuning DNA crosslinking, we modulate condensate dynamics and suppress liquid-to-solid transitions of FUS – a hallmark of disease. These findings demonstrate that multivalent, confined environments fundamentally reshape protein-nucleic acid interactions and phase behavior. The PN platform complements test-tube assays and complex cellular settings and enables to dissect nuclear condensates under controllable conditions.

Introduction

Phase separation (PS) leading to biomolecular condensates plays a key role in cell regulation, organization, and stress response.[1–3] Many of such condensates are formed by protein and nucleic acid components, for instance, the nucleolus, Cajal bodies, paraspeckles, and nuclear speckles in the cell nucleus, and stress granules or P-bodies in the cytoplasm.[4] Understanding such protein/nucleic acid condensates is of critical importance to further our knowledge about disease development and cellular regulatory processes, which is particularly challenging for condensates formed by multiple components and occurring in complex and nucleic acid-rich environments, such as the nucleus.

One key problem is the translatability of facile test-tube solution experiments to *in cellulo* situations.[5] Simple solution investigations benefit from high throughput and widely tunable conditions, and have the potential to speed up mechanistic understanding due to reductionist settings. However, such systems rarely capture the complexity of the cellular environment, which is not only crowded but also compositionally and mechanically heterogeneous. This discrepancy limits the translatability of insights gained from dilute solution assays to real biological function. The addition of molecular crowders has been one approach to arrive at situations mimicking more closely the crowded cellular environment. Nonetheless, some crowders influence PS beyond their crowding contribution,[6,7] partition into condensates[8–10] or change condensate properties at high concentrations.[11] Beyond these limitations, such conditions cannot replicate anything vaguely reminiscent of the nucleus, for which it would be very beneficial to have tunable *ex cellulo* model systems.

A particular gap exists in understanding how nucleic acid sequence, spatial confinement, and material state jointly shape PS of biopolymers – a triad that remains unaddressable thus far in conventional approaches. A system that allows precise control over these factors could provide critical insights into the mechanisms of nuclear PS, especially for proteins that are implicated in disease, such as neurodegenerative diseases and cancer, through misregulated condensation.[12,13]

We hypothesized that a critical cross-fertilization of the field of biological PS would be possible by transferring concepts from all-DNA artificial cells[14–17] to study condensate formation processes in tailored nucleus-mimetic environments. Such synthetic structures are built entirely from DNA and are tunable in composition, structure and viscoelastic properties. To this end, we introduce here a protonucleus (PN) platform as an advanced and versatile test system between classical test tube/solution experiments and *in cellulo* studies. We explore this system for a model protein implicated in neurodegenerative disease – the fused in sarcoma (FUS) protein – which is known to undergo PS and to bind to nucleic acids.[18–21] We find that the recruitment and PS of FUS is not only highly dependent on DNA and RNA sequence, but that classical *ex vivo* methods such as electrophoretic mobility shift assays (EMSA) cannot fully predict the interactions found in crowded and restrained DNA PN environments. Additionally, we show that the dynamic/viscoelastic properties of the PN significantly influence PS of FUS to the point of full suppression. Our new *in protonucleo* method based on a tunable DNA nanoscience approach introduces a highly versatile platform that complements simple in solution *ex vivo* assays and *in cellulo* studies.

Results and Discussion

Synthetic all-DNA protonuclei as a protein PS platform

The protonucleus (PN) builds on our work on DNA-based core-shell particles formed by temperature-induced PS of two long ssDNA multiblock copolymers, namely p(A_{20}-m) and p(T_{20}-n).[15,17,22–24] Therein, A_{20} and T_{20} correspond to homo-repeats of adenine and thymine nucleobases, respectively, and m and n are ssDNA barcodes that allow for functionalization (sequences in Scheme 1a, Table S1). In short, PN form by selective PS of p(A_{20}-m) during heating, whereafter p(T_{20}-n) hybridizes during cooling onto the phase-separated droplets, stabilizing them at the core/shell interface by multivalent A_{20}/T_{20} duplexes (Scheme 1a). The resulting PN has a kinetically trapped, liquid pool of long ssDNA inside. The DNA concentration is 5-13 g/L, which equals well to that of the nucleus in a cell of about 9-31 g/L (Table S2). The PN shell is highly permeable and allows for the uptake of macromolecules, such as proteins.[22]

To apply the PN system to a biologically and disease-relevant model system, we selected the fused in sarcoma (FUS) protein because it is a very well-studied nucleic acid-binding protein.[20,21,25] In cells, FUS is involved in splicing, DNA damage repair, transcription regulation, RNA transport and translation regulation.[26–29] FUS is mostly located in the nucleus of healthy cells, but can be mislocalized to the cytoplasm of nerve cells because of mutations in the nuclear localization signal (NLS), or other defects to Transportin-1 (TNPO1)-mediated nuclear import of FUS (Scheme 1b).[28,30–32] Cytosolic FUS phase separates over time and FUS condensates undergo an irreversible liquid-to-solid transition to a non-functional amyloid-like state,[18,33–35] implicated in neurodegenerative diseases, such as amyotrophic lateral sclerosis (ALS) and frontotemporal dementia (FTD).[36–38]

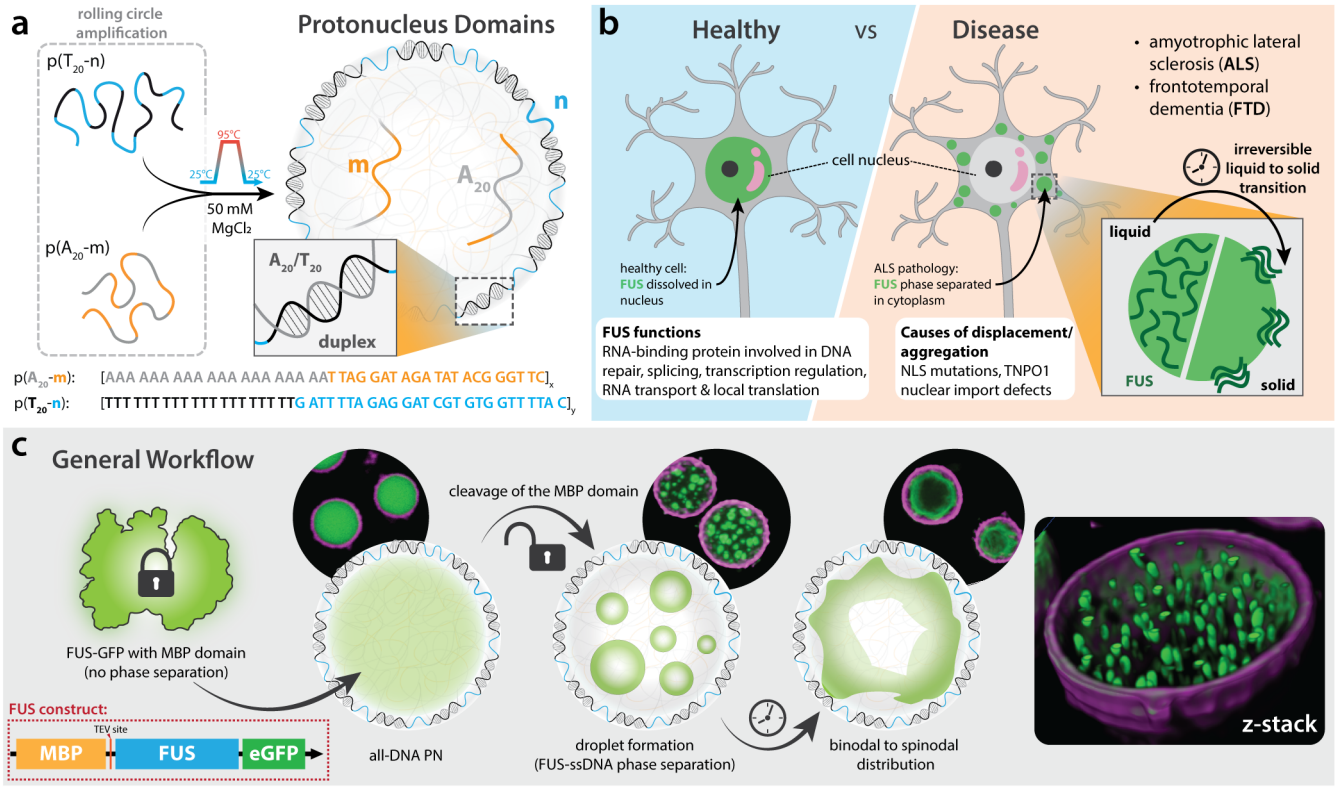

Scheme 1: Protonucleus (PN) platform and biological relevance of FUS phase separation. a) Simplified preparation of our PN platform and the relevant addressable domains m, n and A_{20}. b) Schematic comparison of FUS in a healthy neuron to the FUS pathology in ALS and FTD. c) The general workflow of a phase separation experiment with MBP-FUS-GFP (soluble) and all-DNA PN, encompassing protein loading, MBP-tag cleavage, and microscopic visualization of FUS phase separation inside PN.

Scheme 1c visualizes the general workflow. We use recombinantly produced full-length FUS with a C-terminal eGFP tag for fluorescence imaging by confocal laser scanning microscopy (CLSM), as well as an N-terminal protease-cleavable maltose binding protein (MBP) tag for enhanced solubility and initial suppression of PS. This strategy allows to introduce MBP-FUS-GFP into PN in a soluble state, and once the sample is equilibrated to trigger PS of FUS by cleaving off the MBP tag with TEV protease.

FUS loading ratio controls PS morphology

We first investigate the influence of FUS-GFP concentration on the PS behavior. In these experiments we use pristine PN only labeled at their shell with n*^{Atto565} to visualize the shell in CLSM (magenta channel). The ratio of FUS-GFP to repeating units (r.u.) of p(A_{20}-m) describes the increased loading of FUS-GFP into the PN. Figure 1 depicts four major domain windows that occur at different FUS-GFP/p(A_{20}-m) ratios (0.17 – 1.5). At a low loading ratio (< 0.17), no coarsened phase-separated morphology is visible after removing the MBP solubility tag. This changes drastically when increasing the loading ratio to 0.31

and 0.37, where phase-separated FUS-GFP droplets appear within the PN, resembling a binodal domain. Binodal PS takes place in the metastable boundary region of the phase diagram. It requires fluctuations to nucleate PS, which usually leads to a droplet morphology by growth and coalescence. In contrast, spinodal decomposition happens spontaneously and rapidly for more concentrated solutions in the center of the phase diagram. This typically leads to co-continuous morphologies that coarsen and can also form a single domain at the end of the PS process.[39–42] Interestingly, for loading ratios between 0.61 and 0.72, a co-continuous morphology occurs that is reminiscent of the spinodal domain. Finally, at high ratios above 1 there is no observable coarsened PS, indicating that the loading capacity of the PN is reached and one big condensate forms. This is particularly evident in case of the last sample (Figure 1, right image), where FUS-GFP also accumulates around the shell of the PN in solution.

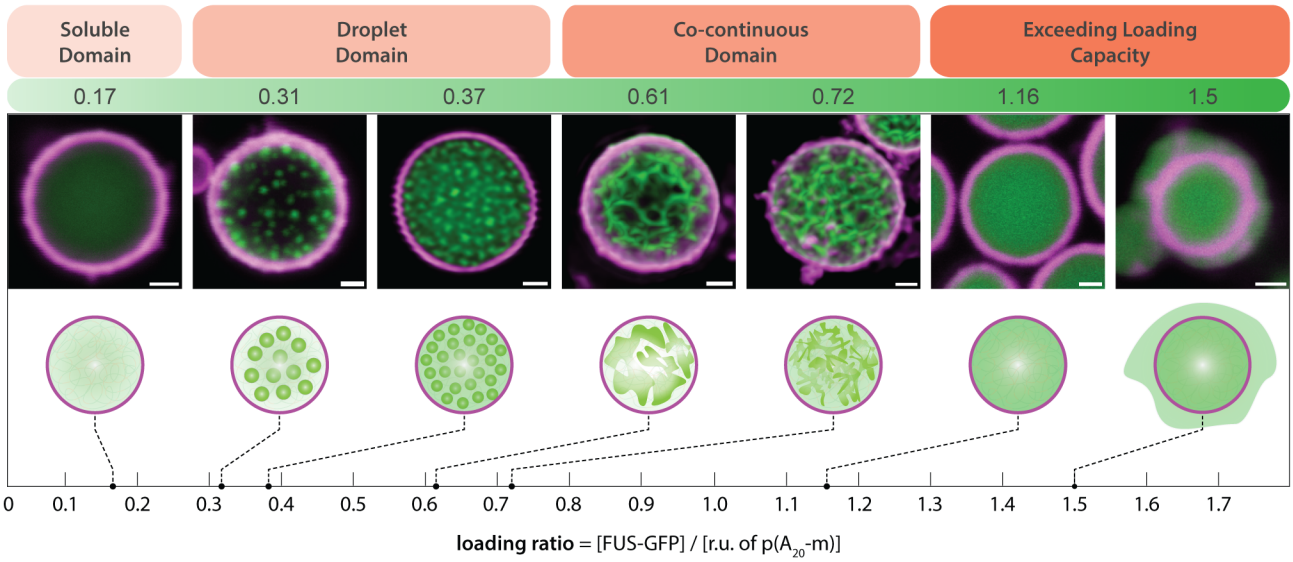

Figure 1: Different ratios of FUS-GFP to core repeating unit of p(A_{20}-m) of protonuclei lead to diverse PS morphologies. The PN shell is shown in the magenta channel, FUS-GFP is in green. Imaging of the samples was done 3-4 hours after TEV addition. CLSM images 0.31, 0.61 and 0.72 are maximum-intensity z-projections, the remaining images show a single confocal plane. Scale bar = 1 µm.

PN core sequence modifications affect FUS partitioning

One of the strengths of the PN system is the ease of functionalizing them with additional nucleic acids (either DNA or RNA oligonucleotides) via their m barcodes or A_{20} domains to understand how variations in PN core composition impact affinity and PS. This is schematically shown at the top of Figure 2a for six samples: The pristine PN (1) is the only sample without core modification, meaning both m and A_{20} domains are not hybridized. This is different for the next two samples, where a sequence complementary to m is added (sequences in Figure 2b): (2) $m^{*Atto647N}$ forms m/$m^{*Atto647N}$ DNA duplexes. (3) m*-RNA^{Cy5} is a complementary RNA leading to an m/m* DNA/RNA duplex with a dangling RNA strand (39 nt in length). The remaining samples are structured analogously, with the difference of utilizing the A_{20} domain for hybridization: (4) $T_{20}^{Atto647N}$ forms a simple $A_{20}/T_{20}^{Atto647N}$ DNA duplex. (5) U_{20}-RNA^{Cy5} forms a A_{20}/U_{20} duplex with a dangling RNA strand. (6) T_{20}-$m^{Atto647N}$ has a dangling m as additional ssDNA overhang, effectively doubling [m] in the PN core. As RNA overhang in both RNA-containing samples, we chose a physiological RNA with high affinity to FUS.[20,43] All experiments use a loading ratio of 0.30, hence a regime where the pristine PN/FUS-GFP system is in the binodal domain (Figure 1). We chose this concentration regime to ensure an excess of the introduced nucleic acid sequences compared to FUS-GFP.

We monitored the evolution of FUS PS over time through CLSM. Figure 2c shows single PN before TEV addition (boxed region) and at different time points after TEV addition (overview images in Figure S1). The mean diameters of all PN range from 3.7 to 4.7 µm (Figure 2d), thus in similar dimensions as human cell nuclei with an average diameter of about 6 µm.[44]

We first quantify the partitioning of MBP-FUS-GFP into PN by comparing the mean GFP intensity inside the PN core with that of the solution (background; Figure 2d). The equilibrated PN show different levels of protein partitioning. Pristine PN (1) and $T_{20}^{Atto647N}$-PN (4) exceed the other samples by far. Both RNA-containing PN (3: m*-RNA^{Cy5}, 5: U_{20}-RNA^{Cy5}) and T_{20}-m^{Atto647N}-PN (6) show moderate MBP-FUS-GFP partitioning, whereas the weakest partitioning is observed for m*^{Atto647N}-PN (2).

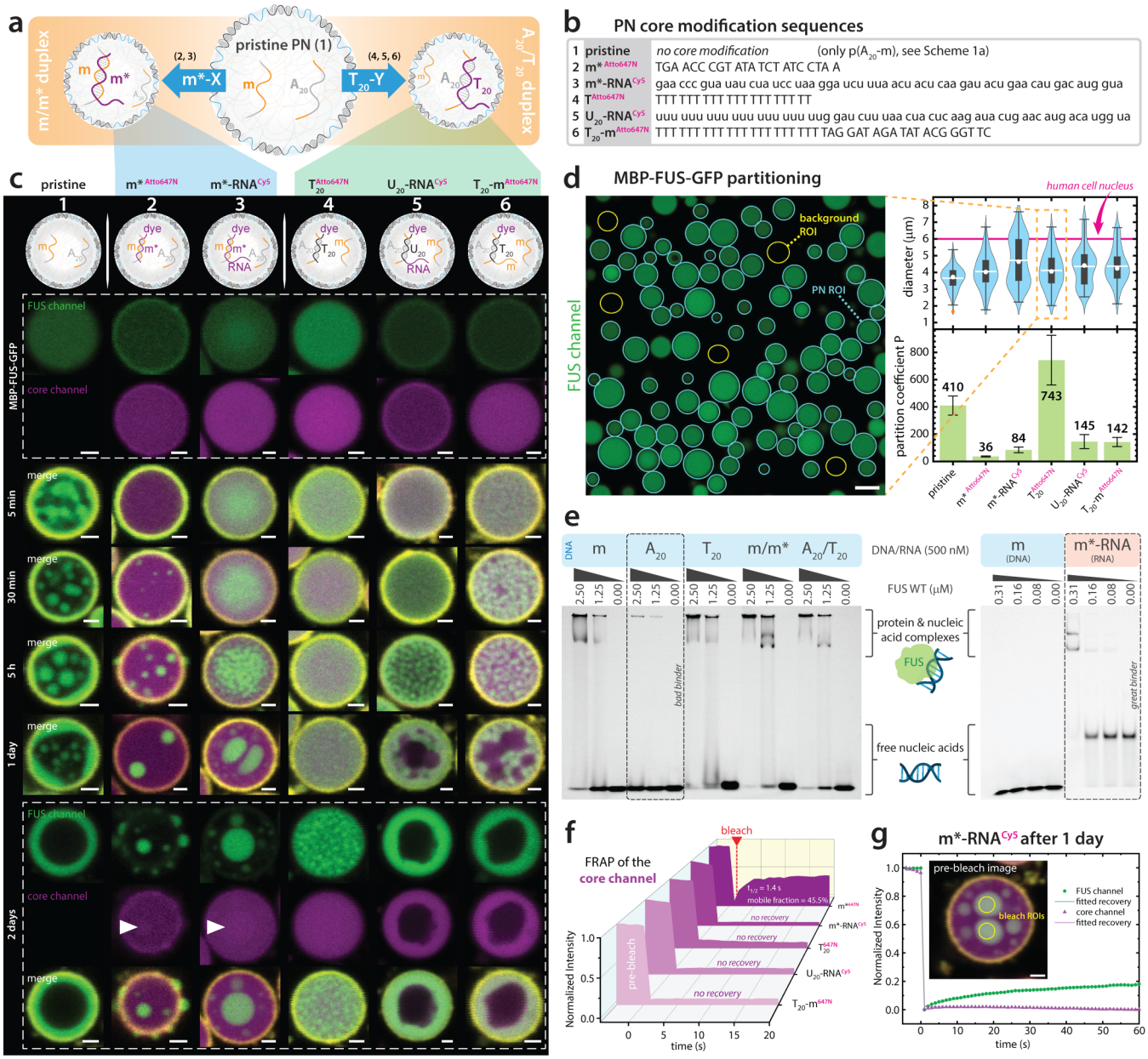

Figure 2: Modification of the PN core sequences alters partitioning and PS behavior. a) Schematic illustration of the two PN core modification strategies used in the experiments. b) DNA (2, 4, 6, uppercase) and RNA (3, 5, lowercase) sequences used for core modification. c) CLSM Snapshots of single PN with different DNA/RNA modifications after defined time intervals of 5 min, 30 min, 5 hours, 1 day and 2 days. FUS-GFP in green, core modifications in magenta and shell in yellow channel. White arrows indicate condensates with core segregation, see Figures S2, S3. All PN have average diameters from 3.7-4.7 µm. We scaled representative PN examples to full panel size for clarity. For overview images with indication of the selected PN, see Figures S4, S5. Scale bar = 1 µm. d) Example of manual PN segmentation in sample $T_{20}^{Atto647N}$-PN to measure PN diameter and partition coefficient P of MBP-FUS-GFP. Scale bar = 5 µm. Violin plots: diameter distribution from 2D CLSM: Box shows inter quartile range (IQR), whiskers to 1.5 x IQR, outliers in orange, mean as white line, median as white circle. Bar chart: Partition coefficient of FUS: Error bars show standard deviation. N = 146, 92, 92, 91, 83, 79 (left to right). e) EMSAs of all relevant DNA/RNA sequences to probe their binding to FUS. f) FRAP of the pA-based core material of the PN of all samples with dye-containing core

modifications before MBP-FUS-GFP addition. Note that the pristine PN (1) does not have a dye modification. g) FRAP of m*RNA^{Cy5}-PN after 1 day for both the core and FUS channel. Scale bar = 1 µm. Loading ratio is 0.30 for all experiments.

Since partitioning is expected to scale with affinity, we semi-quantitatively assessed binding of FUS to the different nucleic acid sequences using electrophoretic mobility shift assays (EMSA, Figure 2e). This analysis demonstrates a moderate affinity of FUS for all DNA sequences except A_{20}, which is a poor FUS binder (Figure 2e, left). A comparison of a moderate binder (m) and a strong binder (3: m*-RNA^{Cy5}) at lower FUS concentration shows the far superior binding affinity of the latter, in line with the known high RNA/FUS affinity for this particular RNA[20,43] (Figure 2e, right).

Comparing the EMSA data to the partitioning data, some trends carry over, such as binding of FUS-GFP is stronger for PN functionalized with RNA sequences such as m*-RNA^{Cy5} (3), U_{20}-RNA^{Cy5} (5) compared to PN simply functionalized with m*^{Atto647N} (2). However, other EMSA results are in stark contrast to the partitioning data. Pristine PN (1) and $T_{20}^{Atto647N}$-PN (4) do not carry the strongly binding RNA sequence and yet show the highest partitioning values. Most interestingly, m/m*^{Atto647N} (2) shows high binding affinity in EMSA, but the lowest partitioning on the PN level. The highest partitioning can be found for $T_{20}^{Atto647N}$-PN (4) with pristine m barcode, but with hybridized A_{20}/T_{20} sequences. Taken together, these experiments highlight for the first time the impact of environmental parameters on nucleic acid/FUS interactions. Most critically, standard in solution EMSA affinity measurements deliver in parts completely different interaction maps compared to the crowded and DNA-rich PN environment. The most significant disparity can be identified for the comparison of $T_{20}^{Atto647N}$ (4, P = 743) and m*^{Atto647N} (2, P = 36) with a ca. 20-fold difference in partitioning (Figure 2d), although both duplexes display similar EMSA affinities (Figure 2e, columns A_{20}/T_{20} and m/m*).

PN core modifications alter dynamics and condensate morphology

Next, we turn to kinetic details of FUS-GFP PS in these differently functionalized PN, after initiating PS by cleavage of the MBP-tag with TEV protease. In pristine PN (1), PS starts quickly, with FUS-GFP droplet formation occurring within five minutes after MBP cleavage and subsequent wetting of the inner surface of the PN shell after a few hours (Figure 2c, left). Additionally, the remaining droplets increase in size due to coalescence. Over the course of 1-2 days the wetting region gains in thickness due to coalescence of FUS-GFP droplets with the FUS-GFP shell. We further comment on the formation of the concentric shell below for dye-labeled PN.

Introduction of m*^{Atto647N} (2) leads to key differences in the PS behavior of FUS-GFP. Hardly any FUS-GFP droplets form in the initial 30 minutes after TEV cleavage within the PN. Afterwards droplets are formed inside and on the outside surface of the PN. Note, that m*^{Atto647N} (2) visualizes the PN core material (magenta channel) and shows a uniform distribution in the time series. Despite low partitioning and bad FUS-GFP retention (compare Figures S6 and S7), the final image shows colocalization of the FUS-GFP droplets and the core material (single channel images: Figures S2 and S3), indicating that p(A_{20}-m/m*^{Atto647N}) chains co-segregate with the FUS-GFP condensates.

For the other samples, FUS-GFP PS progresses more slowly. This is not only due to chemical interactions, but also due to decreased core dynamics as identified by fluorescence recovery after photobleaching (FRAP) of all modified PN before MBP-FUS-GFP addition (Figure 2f). m*^{Atto647N}-PN (2) show a FRAP recovery with $t_{1/2}$ = 1.4 s (Movie 1), whereas all other modified PN do not show any appreciable recovery. The reason for the low dynamics in the RNA-containing samples is the fact that the dangling RNA strand is in fact a hairpin that can also dimerize at high concentrations inside the PN instead of only folding intramolecularly in dilute solution (Table S1, also containing NUPACK structures of dimers). In terms of structure formation, in m*-RNA^{Cy5}-PN (3), the FUS-GFP condensates form in the center of the PN and do not show wetting of the inner surface of the shell as in pristine PN (1). In direct comparison to the m*^{Atto647N}-PN (2), the addition of dangling RNA prevents leakage of the FUS-GFP condensates or formation of droplets at the outside of the shell. Overall, the retention of FUS-GFP after 5 h is much higher for the RNA-containing m*-RNA^{Cy5}-PN (3) than for m*^{Atto647N}-PN (2). The FUS-GFP condensates still behave dynamically as seen from the droplets merging from 5 h to 2 days, even though FUS-GFP and PN core material clearly form a combined phase. This observation is supported by FRAP measurement of the phase-separated droplets (Figure 2g), showing a

178 moderate recovery of FUS-GFP after 1 day, while the core channel remains non-dynamic. This means that FUS-GFP
179 condensate droplets can exchange RNA partners in the core allowing for diffusion inside the PN core.

180 The remaining samples (4: $T_{20}^{\mathrm{Atto647N}}$, 5: U_{20}-RNA^{Cy5}, 6: T_{20}-m^{Atto647N}) are dominated by slow core dynamics. In all cases the
181 phase separated FUS-GFP forms interconnected networks within the PN, which is an unusual behavior for the minority phase.
182 It is a prime example of viscoelastic phase separation (VPS) known from polymer physics, which is caused by a dynamic
183 asymmetry of two components in a mixture, here the long ssDNA in the PN core and FUS-GFP.[45] This dynamic asymmetry
184 leads to the slower phase sustaining mechanical stress, which results in the formation of network-like morphologies instead of
185 droplets. For $T_{20}^{\mathrm{Atto647N}}$-PN (4), the phase separated structure remains arrested within two days, whereas for U_{20}-RNA^{Cy5} (5)
186 and T_{20}-m^{Atto647N} (6) PN, this VPS-network relaxes slowly over the span of two days. Here, the affinity of FUS-GFP to the PN
187 material is strong enough to induce co-phase-segregation. This leads to vacuole formation, with the condensate being
188 segregated to the PN shell. The formation of the concentric shell is due to affinity of the pA core material with the pT shell
189 (A_{20}/T_{20}-duplexes stabilize the PN core shell interface). The similarity in the final morphology compared to pristine PN (1)
190 raises the question whether the pA core material of the pristine PN is segregated as well. Indeed, a covalently labelled p(A_{20}-
191 m)^{Atto425} shows a similar co-segregation (Figure S8). At first glance, this A_{20}/T_{20}-duplex driven morphology seems unique to
192 PN, yet it bears remarkable resemblance to nuclear organization in cells. Cell nuclei are organized by spatially segregated
193 euchromatin and heterochromatin domains, with the latter located at the nuclear periphery. This structure results from tethering
194 of heterochromatin to nuclear lamina, which are rooted in the inner nuclear membrane.[46,47] Accordingly, PN replicate this
195 tethering-guided nuclear compartmentalization in a minimalist model system.

196 In summary, FUS-GFP partitioning, PS timescale and condensate morphology are drastically influenced by the nucleic acid
197 sequences present in the PN core. Simple sequence variations lead to the extremes of slowed down PS kinetics
198 (4: $T_{20}^{\mathrm{Atto647N}}$), partial expulsion of FUS-GFP from the core (2: m*^{Atto647N}) and full co-phase-segregation of FUS-GFP with the
199 PN core material (1: pristine, 5: U_{20}-RNA^{Cy5}, 6: T_{20}-m^{Atto647N}). Critically, classical EMSA affinity measurements largely failed
200 to predict the observed complex system behavior. This disparity underscores a central insight of our study: Protein/nucleic acid
201 affinity alone cannot predict PS behavior in confined, crowded, and multivalently interacting PN environments. Instead, the
202 dynamic and structural context in which these interactions occur plays a decisive role. The origin relates to the fact that the PN
203 permits multimodal binding in a compact, electrostatically diverse space, instead of an isolated binary interaction. For instance,
204 high affinity binders like m*-RNA^{Cy5} (3, Figure 2e) cause strong multimodal binding which restricts the degrees of freedom of
205 the protein by locking its orientation. In contrast to this restricted conformation, a weak binder will offer conformational
206 freedom to the protein, allowing it to more dynamically interact with an environment phase and adapt to its constraints. We
207 hypothesize that these weak, transient interactions provide a better environment for partitioning in crowded systems. While our
208 results indicate intricate and complex interplays between many parameters, they clearly show that test-tube affinity
209 measurements have limitations in replicating the processes in crowded DNA-rich environments, highlighting the importance
210 of developing PN to better mimic intra-nuclear complexity.

211 **FUS PS is controlled by PN core crosslinking**

212 Next to tuning the composition, another key advantage of our PN platform is the ability to tune their dynamic and viscoelastic
213 properties. This can be achieved by using a modified p(A_{20}-m-XL) sequence, which contains a self-complementary region XL
214 that forms crosslinks (Figure 3 inset). Such linkers are known to profoundly impact the viscoelastic properties as well-
215 established for macroscopic DNA hydrogels.[48,49] Mixing p(A_{20}-m-XL) with p(A_{20}-m) prior to the formation of the PN leads to
216 co-assembly within the PN, allowing to fine-tune their composition. FRAP measurements after MBP-FUS-GFP partitioning
217 reveal a great impact of the XL domain on PN dynamics (Figure S9). The characteristic $t_{1/2}$ increases for higher p(A_{20}-m-XL)
218 fractions and the mobile fraction decreases, confirming the intended decrease in PN core dynamics for higher XL amounts.

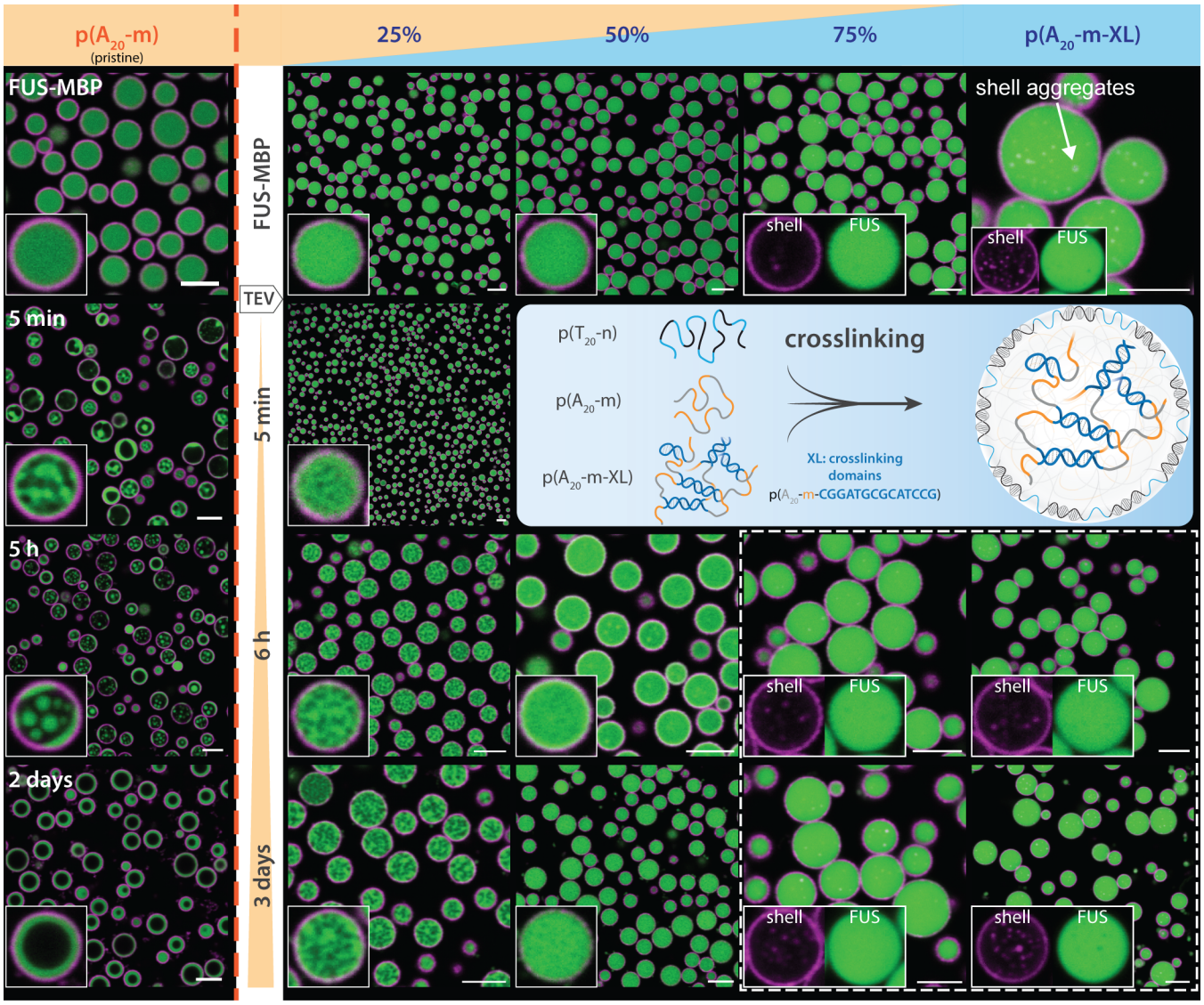

Figure 3: Crosslinking PN influences FUS PS. Various degrees of crosslinking can be achieved by adding different fractions of p(A_{20}-m-XL) to the PN (loading ratio = 0.30). XL forms self-complimentary crosslinks. Both highly crosslinked samples (75% and 100%) show some magenta speckles in the PN core, which originate from some shell aggregates present before TEV addition. The dashed square in the bottom right indicates a region of no visible phase separation within the optical limits of the microscope. A corresponding FRAP experiment is shown in Figure S9. Scale bars: 5 µm.

A clear trend emerges how crosslinking affects FUS PS in PN after addition of TEV protease. Non-crosslinked, pristine PN with pure p(A_{20}-m) display quick FUS PS and droplet formation that reorganizes over the course of 2 days to a concentric shell (same data as seen in Figure 2c). These dynamics are greatly reduced when adding 25% p(A_{20}-m-XL), which changes both the PS morphology and time progression. Grainy FUS PS is visible after 5 min, which only slightly coarsens during the next 3 days. Instead of localizing at the inner shell, a spongy and arrested phase-separated network occurs that originates from VPS.[45] A further increase of crosslinker leads to even slower dynamics. For 50% p(A_{20}-m-XL), FUS PS is barely visible after 6 h and does not progress much over the next 3 days. Finally, at 75% crosslinking and above, no microscopically visible FUS PS occurs anymore over the span of 3 days.

Viscoelastic environment suppresses FUS liquid-to-solid transitions

As commonly reported for FUS, condensates can age and undergo a liquid-to-solid transition over time.[18,19,50–52] Our PN with tunable dynamics can help to understand how confinement can influence this behavior. FUS condensate liquid-to-solid

transition is measurable by FRAP of the pristine p(A_{20}-m)-PN without crosslinking by the consecutive decrease in the FRAP recovery profiles (FUS channel; Figure 4a). For PN with p(A_{20}-m-XL)/p(A_{20}-m) = 75/25, hence at highly crosslinked state, the initial FRAP of FUS-GFP shows lower recovery dynamics due to the highly crosslinked nature of the PN. However, as time progresses, further liquid-to-solid transition of FUS condensates is suppressed, as the decrease of the FRAP profiles is comparably little in highly cross-linked PN (Figure 4a).

To further underscore the dynamic properties of FUS-GFP in the 75% crosslinked PN, we added a two-fold excess of m*-RNA^{Cy5} to offer FUS-GFP a non-polymeric binder after 4 days of aging inside the PN (Figure 4b). This control experiment is designed to discern liquid FUS from solid fractions, as we hypothesized that non-solidified FUS would interact and phase-segregate with a dynamic nucleic acid binder. Over the course of a few hours, the m*-RNA^{Cy5} infiltrates the core of the aged, 75% crosslinked PN (Figure 4c). However, because of the two-fold excess there is a large unbound fraction of m*-RNA^{Cy5} in solution, so that FUS-GFP condensates emerge out of the PN with only a low intensity in the green FUS channel remaining inside PN. We suggest that the residual FUS-GFP in the PN core largely originates from the solid fraction, whereas the dynamic, RNA-bound fraction is leached out and forms condensates on the outer surface of the PN shell. Taken together, the viscoelastic suppression of FUS-GFP PS also slows down the aberrant liquid-to-solid transition of the protein – a hallmark of desease. Hence, the viscoelastic properties are not only relevant to enter the domain of VPS (FUS network formation, although at binodal concentrations), but also to regulate the dynamics of FUS PS and its liquid-to-solid transition during aging. These results are instructive for possible therapeutic strategies, as they highlight the importance of the physical environment of membraneless organelles for aberrant phase transition and protein aggregation processes.

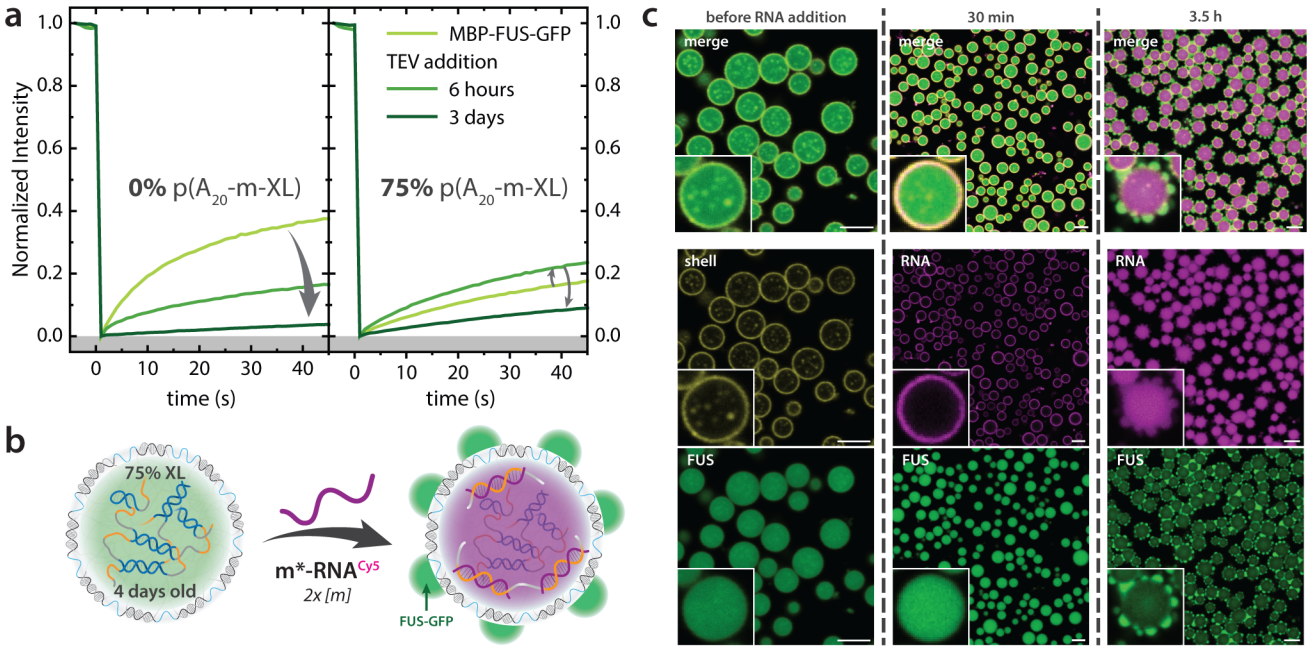

Figure 4: FUS-GFP in 75% crosslinked sample (75% p(A_{20}-m-XL)) remains dynamic after 4 days. a) FRAP measurements in the FUS-GFP channel in 0% and 75% crosslinked PN samples over time after MBP-FUS-GFP addition (light green line), and at two time points after TEV protease induced phase separation (darker green lines). b,c) FUS-GFP is drawn out of 75% XL-PN after addition of excess m*-RNA^{Cy5} to a 4 days old PN sample. Scale bars = 5 µm.

Conclusions

This work has introduced protonuclei (PN) – programmable DNA-based nucleus-mimicking compartments – as a versatile platform to study the impact of environmental constraints on the affinity, phase separation, and liquid-to-solid phase transitions

of nucleic acid-binding proteins. Our findings give a new perspective on how to interpret protein-nucleic acid interactions and PS in the context of more complex cell-like environments, here in particular the cell nucleus. While affinity-based assays remain useful, they fail to reflect the complex interplay of multivalency, confinement, and physical state that governs condensation in the nucleus. The PN system and future derivates thereof have the potential to fill this gap, offering a controllable testbed that reveals how local context shapes condensate formation, retention, and aging. By mimicking essential features of the cell nucleus, including nucleic acid crowding, compositional heterogeneity, and tunable viscoelasticity, PN provide a new intermediate between simplistic *ex vivo*/*test tube* assays and complex cellular systems. Using FUS, a protein linked to neurodegenerative diseases, we demonstrated that phase behavior of this protein inside PN is strongly influenced by the sequence and structure of nucleic acids, as well as by the dynamic mechanical properties of the DNA-rich core.

A central finding is the limited predictive power of solution-based protein-nucleic acid interaction assays, such as EMSA, which fail to capture the complex interactions arising in the multivalent and crowded PN environment. We show here that seemingly minor changes in nucleic acid sequence or mechanical constraints can have drastic effects on protein partitioning, phase morphology, and condensate dynamics. Moreover, by incorporating crosslinks into the PN core, we demonstrated how viscoelasticity can suppress PS and delay the liquid-to-solid transition during condensate aging – pointing to a critical role of the physical environment in regulating phase behavior. The ability of PN to suppress PS or alter condensate morphology via crosslinking parallels the influence of chromatin compaction[53] or nuclear stiffness[54] on modulating nuclear PS in cells, pointing to potential physical regulators of phase transitions beyond biochemical interactions. These insights support emerging views that pathological phase transitions may be mitigated not only by molecular inhibitors but also by targeting the mechanical properties of the nuclear environment.[55]

Looking ahead, the PN system offers a powerful framework to probe more complex nuclear PS phenomena. Its modularity allows incorporation of multiple proteins and nucleic acids, enabling studies of competition, cooperativity, and emergent behavior. The ability to systematically vary protein variants and nucleic acid sequences also opens up new routes to explore disease-associated mutations and their impact on phase transitions in a nucleus-like environment. Additionally, future development of a theoretical model to predict protein PS in PN can be an insightful tool to identify the underlying molecular interactions governing partitioning, dynamics, morphology and PS suppression. Beyond structural observations, PN can be adapted to investigate the functional consequences of PS, for example on transcription or RNA processing. Given their synthetic nature and programmability, PN may also serve as bottom-up tools for screening condensate-modulating compounds, or as functional components in synthetic biology systems.

In the long term, the PN platform could aid in reconstituting complex, disease-relevant membraneless organelles under tunable conditions. This might allow systematic dissection of how disease-linked mutations, co-factors, or mechanical perturbations influence phase behavior – a task that remains challenging in live cells. As synthetic biology and condensate pharmacology advance, synthetic systems like PN may also help screen for compounds that modulate phase behavior not just by disrupting binding, but by altering the physical microenvironment. Altogether, our findings not only highlight the limitations of classical assays but also provide a blueprint for powerful *ex vivo* models. PN offer a rich design space to dissect the rules of intracellular PS and hold promise for guiding future therapeutic strategies targeting condensate dynamics in disease.[56,57]

Methods

Materials

Oligonucleotide strands were ordered as shown in Table S1 from Integrated DNA Technologies (IDT) and Biomers. Enzymes phi29 DNA Polymerase (10 U μL^{-1}), T4 DNA Ligase (2 U μL^{-1}), Exonuclease I (20 U μL^{-1}), Exonuclease III (200 U μL^{-1}) were purchased from LGC Genomics. Thermostable inorganic pyrophosphatase (TIPP, 2000 U μL^{-1}) and nuclease-free water were purchased from New England Biolabs (NEB), dNTPs (100 mM - 110 mM) were purchased from Jena Bioscience. Sodium

303 chloride (Gen-Apex) was purchased from VWR, magnesium chloride solution (2M, BioUltra) was purchased from Sigma
304 Aldrich, Invitrogen TE buffer (10 mM Tris, 1 mM EDTA, pH 8.0) was purchased from Thermo Fisher Scientific.

305 **PN core and shell ssDNA synthesis**

306 The procedure for rolling circle amplification of ssDNA polymers was adapted from our previous report.[23] The stock solutions
307 of 5′-phosphorylated templates and their corresponding ligation strand (Table S1) were mixed in equimolar stoichiometry to
308 attain a final concentration of 1 μM in TE buffer (Invitrogen; 10 mM Tris(hydroxymethyl)aminomethane pH = 8 and 1 mM
309 EDTA) containing additionally 100 mM NaCl (total volume 100 μL). The concentrations of the strands are kept low to prevent
310 inter-strand hybridizations. The buffered mixture was heated up to 85 °C (for 5 min) at a rate of 3 °C s^{-1} and slowly cooled
311 down to 25 °C at 0.01 °C s^{-1}. After annealing the strands, 20 μL of 10x commercial ligase buffer (LGC; 500 mM Tris-HCI,
312 100 mM $MgCl_2$, 50 mM dithiothreitol, and 10 mM ATP), 70 μL of water, and 10 μL of T4 ligase (2 U μL^{-1}) were added in the
313 reaction tube containing 100 μL of the template strand, stirred (10 min, 400 rpm) and left to react for 3 h at 25 °C. The T4
314 ligase was then denatured by heating the reaction mixture for 20 min at 70 °C. Then 10 μL of exonuclease I (LGC; 40 U μL^{-1})
315 and 10 μL of Exonuclease III (LGC; 200 U μL^{-1}) were added, and the mixture was kept overnight at 37 °C on a thermo-shaker
316 (Eppendorf) with gentle shaking (300 rpm) to digest unreacted ligation strands and non-circularized templates in solution. Then
317 the exonucleases were subsequently deactivated by heating the reaction mixture at 80 °C for 40 min. The circular templates
318 were purified using the Amicon Ultra-centrifugal filters with a 10 kDa cut-off (Merck Millipore) and washed three times using
319 TE buffer over the same filter. The concentration of circular templates was measured by the use of a ScanDrop (Jena Analytic)
320 spectrophotometer, and the solutions were diluted to 10 μM using TE buffer. To synthesize multiblock ssDNA polymers, 0.5
321 μL circular template (10 μM) were mixed with 10 μL of commercial 10x polymerase buffer (LGC; 500 mM Tris-HCl, 100 mM
322 $(NH_4)_2SO_4$, 40 mM Dithiothreitol, 100 mM $MgCl_2$), 1 μL of exonuclease resistant primer (10 μM in TE buffer), 2 μL of Φ29
323 Polymerase (LGC; 10 U μL^{-1}), 5 μL of pyrophosphatase (New England Biolabs; 2000 U μL^{-1}), and 5 μL of an adjusted dNTP
324 mixture (total dNTP concentration of 5 mM, the percentage of each base correspond to the expected sequence composition in
325 the ssDNA polymer), and 76.5 μL of ultrapure nuclease-free water. The reaction mixtures were kept at 30 °C for 60 h on a
326 thermo-shaker with a gentle shaking (300 rpm). The solution containing ultralong ssDNA polymer was subjected to
327 temperature-induced cleavage for 15 min at 95 °C, and the resulting solution was then washed through Amicon Ultra-
328 centrifugal filters with a 30 kDa cut-off (Merck Millipore, three to four times) using 350 μL of TE buffer. The amount and
329 purity of the ssDNA polymers were determined using a ScanDrop (Jena Analytic) spectrophotometer. The pyrophosphatase
330 enzyme was added to prevent the formation of insoluble magnesium pyrophosphate as a side product that hinders the
331 polymerization process and is also accountable for resulting in so-called nanoflowers and might cause misperception during
332 the microscopic investigations.

333 **Purification of MBP-FUS-EGFP-His_6 and MBP-FUS-His_6**

334 Expression and purification of recombinant MBP-FUS-EGFP-His_6 and MBP-FUS-His_6 was performed as described in
335 (Hofweber, Cell 2018)[52]. Briefly, BL21-DE3-Rosetta-LysS cells were transformed with a pMal-MBP-Flag-FUS-GFP-His_6 or
336 MBP-FUS-His_6 expression plasmid and grown in standard lysogeny broth (LB) medium until OD (600 nm) value reached 0.8.
337 Expression was induced with 0.1 mM IPTG for 22 h at 12 °C. Cells were lysed in lysis buffer (50 mM Na_2HPO_4/NaH_2PO_4 pH
338 8.0, 300 mM NaCl, 10 μM $ZnSO_4$, 40 mM imidazole, 4 mM β-mercaptoethanol, 10 % (v/v) glycerol and 1 μg/ml each aprotinin,
339 leupeptin and pepstatin) using sonication. MBP-FUS-GFP-His_6 or MBP-FUS-His_6 were purified by tandem-affinity
340 purification using Ni-NTA agarose (Qiagen) and amylose resin (NEB) and eluted in lysis buffer supplemented with 250 mM
341 imidazole and 20 mM maltose for MBP-FUS-EGFP-His_6, and 50 mM imidazole and 10 mM maltose for MBP-FUS-His_6,
342 respectively. Proteins were dialyzed against storage buffer (20 mM Na_2HPO_4/NaH_2PO_4, pH 8.0, 150 mM NaCl, 5% (v/v)
343 glycerol, 1 mM EDTA, 1 mM DTT), snap-frozen in liquid N_2 and stored at -80°C. The OD260/280 ratio for MBP-FUS-EGFP-
344 His_6 was 0.74, and for MBP-FUS-His_6 was 0.65.

345 **His_6-TEV protease purification**

346 Expression and purification of His_6-Tev was performed as described in (Hofweber, Cell 2018)[52]. Briefly, BL21-DE3 Rosetta-
347 LysS cells were transformed with a pET24(+)-His-Tev plasmid and grown in standard lysogeny broth (LB) medium until OD
348 (600 nm) value reached 0.7. Expression was induced with 0.5 mM IPTG for 20 h at 18 °C. Cells were lysed in lysis buffer (50
349 mM Tris pH8, 200 mM NaCl, 20 mM imidazole, 10% (v/v) glycerol, 4 mM β-mercaptoethanol) in presence of 0.1 mg/ml
350 RNase A using lysozyme and sonication. His_6-Tev was purified using Ni-NTA agarose (QIAGEN) and eluted in lysis buffer
351 containing 600 mM imidazole. The protein was dialyzed against storage buffer (50 mM Tris pH8, 150 mM NaCl, 20% (v/v)
352 glycerol, 2 mM DTT), snap-frozen in liquid N_2 and stored at -80°C.

353 **PN formation**

354 PN are formed as shown in Scheme 1a. The formation of PN is initiated by combining pA at 0.18 g/L and pT at 0.03 g/L in TE
355 buffer, together with $MgCl_2$ at a final concentration of 50 mM. A typical preparation would target a final volume of 65 µL in a
356 PCR tube, which is enough for 6 experimental batches. The mixture is then subjected to a heating ramp to 95°C for 20 min
357 with a heating and cooling rate of $3°Cmin^{-1}$. After cooling the sample is split up and 10 µL of the PN stock are added to a fresh
358 PCR tube containing the respective dye-labelled DNA or RNA strands. Here, the DNA complementary to the shell (n*) is
359 added in exact stoichiometry to the barcode concentration, whereas the core DNA or RNA (m*) is added with a dilution factor
360 of 0.8 to ensure there is none left in solution. After mixing with a pipette, the samples are allowed to equilibrate for 60 minutes
361 while shaking at 400 rpm. In a final step the buffer is adjusted to FUS-nucleic acid binding buffer by 10x dilution with HEPES
362 buffer (10 mM HEPES, 200 mM KCl, 1 mM DTT, 5 mM $MgCl_2$, Glycerol 3%, pH 7.5) in a well plate, yielding a final Mg^{2+}
363 concentration of 10 mM. The PN are then allowed to swell and settle to the bottom of the plate, so that the volume can be
364 carefully reduced with a pipette from the top to a working volume of 25 µL.

365 For crosslinked PN the specified fraction of pA was replaced by pA-XL with a self-complementary domain, but all other steps
366 of the preparation remain the same.

367 **Concentration-dependent PS experiments**

368 PN were prepared via heating ramp as mentioned previously, then shell dye $n^{*Atto565}$ was added and the sample equilibrated for
369 1 h. Afterwards the PN were centrifuged at 9000 rpm for 5 min to sediment them. The TE buffer was discarded and the PN
370 were re-dispersed in droplet buffer (20 mM Na-Phosphate, pH 7.5, 75 mM NaCl, 2.5% glycerol, 1 mM DTT) by gentle shaking
371 at 400 rpm for 2 hours. Afterwards, FUS was added as specified, after 30 minutes TEV was added to the samples in 2.7 eq to
372 FUS-GFP. Imaging of the samples was done 3-4 hours after TEV addition. The CLSM images 0.31-0.72 have been
373 deconvoluted with Leica Lightning software, images 0.31, 0.61 and 0.72 are maximum-intensity z-projections (Fiji software[58]).
374 All images have been adjusted in contrast and brightness.

375 **PN core modification experiments and crosslinking**

376 A fresh aliquot of the MBP-FUS-GFP protein (45 µM) was thawed slowly on ice and mixed gently with a pipette. It was then
377 added at a final concentration of 1.5 µM to the respective PN microplate well with a pipette and immediately mixed with a
378 bigger volume pipette to ensure an even distribution. The protein was allowed to partition into the PN for 30-60 min at room
379 temperature until completion of partitioning was confirmed via CLSM. Then a freshly thawed aliquot of TEV protease (80
380 µM) was mixed and added to the wells at a final concentration of 5 µM, marking the start of the PS process. After all additions
381 were made, the plate was sealed to avoid evaporation within the timespan of the experiment.

382 **Electrophoretic Mobility Shift Assay (EMSA)**

383 The nucleic acid sequences, modifications and suppliers can be found in Table S1. Duplexes ($m/m^{*Atto647N}$ and $A_{20}/T_{20}^{Atto647N}$)
384 were annealed using one labelled strand and one unlabelled strand. 500 nM of labelled nucleotide probe were diluted in binding
385 buffer (20 mM Na-Phosphate pH 7.5, 75 mM NaCl, 5 mM $MgCl_2$, 2.5 % Glycerol,1 mM DTT, 1 U/µl RNase inhibitor (Thermo
386 Fisher)) and mixed with varying amounts of MBP-FUS-His_6. Binding reactions (10 µl) were incubated for 1 h at RT and after

387 addition of 2 µl 30% (v/v) glycerol samples were loaded onto a 1 mm thick non-denaturing polyacrylamide gel (6%) in 0.5 x
388 TBE. Gels were run at 100 V for 40 min at RT before imaging with a Bio-Rad ChemiDoc MP Imaging system.

389 Acknowledgements

390 We acknowledge funding from CRC1551 'Polymer Concepts in Cellular Function' of the Deutsche Forschungsgemeinschaft
391 (DFG project number 464588647). Dorothee Dormann acknowledges funding by the DFG Heisenberg programme (DFG
392 project number 442698351). We would like to thank Prof. Dr. Miguel Andrade for his helpful discussions.

393 Declaration of Interests

394 The authors declare no competing interests.

395 Abbreviations

396	ALS	amyotrophic lateral sclerosis
397	CLSM	confocal laser scanning microscopy
398	DNA	deoxyribonucleic acid
399	eGFP	enhanced green fluorescent protein
400	EMSA	electrophoretic mobility shift assay
401	FTD	frontotemporal dementia
402	FUS	fused in sarcoma protein
403	IDR	intrinsically disordered region
404	MBP	maltose binding protein
405	NLS	nuclear localization signal
406	PN	protonucleus / protonuclei
407	PS	phase separation
408	RNA	ribonucleic acid
409	TEV	Tobacco Etch Virus protease
410	VPS	viscoelastic phase separation

411 References

412 1. Hyman, A.A., Weber, C.A., and Jülicher, F. (2014). Liquid-Liquid Phase Separation in Biology. Annu. Rev. Cell Dev.
413 Biol. *30*, 39–58. https://doi.org/10.1146/annurev-cellbio-100913-013325.

414 2. Banani, S.F., Lee, H.O., Hyman, A.A., and Rosen, M.K. (2017). Biomolecular Condensates: Organizers of Cellular
415 Biochemistry. Nat. Rev. Mol. Cell Biol. *18*, 285–298. https://doi.org/10.1038/nrm.2017.7.

416 3. Boeynaems, S., Alberti, S., Fawzi, N.L., Mittag, T., Polymenidou, M., Rousseau, F., Schymkowitz, J., Shorter, J., Wolozin,
417 B., Van Den Bosch, L., et al. (2018). Protein Phase Separation: A New Phase in Cell Biology. Trends Cell Biol. *28*, 420–
418 435. https://doi.org/10.1016/j.tcb.2018.02.004.

419 4. Hirose, T., Ninomiya, K., Nakagawa, S., and Yamazaki, T. (2023). A Guide to Membraneless Organelles and Their
420 Various Roles in Gene Regulation. Nat. Rev. Mol. Cell Biol. *24*, 288–304. https://doi.org/10.1038/s41580-022-00558-8.

421 5. Alberti, S., Gladfelter, A., and Mittag, T. (2019). Considerations and Challenges in Studying Liquid-Liquid Phase
422 Separation and Biomolecular Condensates. Cell *176*, 419–434. https://doi.org/10.1016/j.cell.2018.12.035.

423 6. Ghosh, A., Mazarakos, K., and Zhou, H.-X. (2019). Three Archetypical Classes of Macromolecular Regulators of Protein
424 Liquid–Liquid Phase Separation. Proc. Natl. Acad. Sci. *116*, 19474–19483. https://doi.org/10.1073/pnas.1907849116.

7. André, A.A.M., and Spruijt, E. (2020). Liquid–Liquid Phase Separation in Crowded Environments. Int. J. Mol. Sci. *21*, 5908. https://doi.org/10.3390/ijms21165908.

8. Marianelli, A.M., Miller, B.M., and Keating, C.D. (2018). Impact of Macromolecular Crowding on RNA/Spermine Complex Coacervation and Oligonucleotide Compartmentalization. Soft Matter *14*, 368–378. https://doi.org/10.1039/C7SM02146A.

9. Schuster, B.S., Reed, E.H., Parthasarathy, R., Jahnke, C.N., Caldwell, R.M., Bermudez, J.G., Ramage, H., Good, M.C., and Hammer, D.A. (2018). Controllable Protein Phase Separation and Modular Recruitment to Form Responsive Membraneless Organelles. Nat. Commun. *9*, 2985. https://doi.org/10.1038/s41467-018-05403-1.

10. André, A.A.M., Yewdall, N.A., and Spruijt, E. (2023). Crowding-Induced Phase Separation and Gelling by Co-Condensation of PEG in NPM1-rRNA Condensates. Biophys. J. *122*, 397–407. https://doi.org/10.1016/j.bpj.2022.12.001.

11. Kaur, T., Alshareedah, I., Wang, W., Ngo, J., Moosa, M.M., and Banerjee, P.R. (2019). Molecular Crowding Tunes Material States of Ribonucleoprotein Condensates. Biomolecules *9*, 71. https://doi.org/10.3390/biom9020071.

12. Alberti, S., and Dormann, D. (2019). Liquid–Liquid Phase Separation in Disease. Annu. Rev. Genet. *53*, 171–194. https://doi.org/10.1146/annurev-genet-112618-043527.

13. Boija, A., Klein, I.A., and Young, R.A. (2021). Biomolecular Condensates and Cancer. Cancer Cell *39*, 174–192. https://doi.org/10.1016/j.ccell.2020.12.003.

14. Samanta, A., Baranda Pellejero, L., Masukawa, M., and Walther, A. (2024). DNA-Empowered Synthetic Cells as Minimalistic Life Forms. Nat. Rev. Chem. *8*, 454–470. https://doi.org/10.1038/s41570-024-00606-1.

15. Merindol, R., Loescher, S., Samanta, A., and Walther, A. (2018). Pathway-Controlled Formation of Mesostructured All-DNA Colloids and Superstructures. Nat. Nanotechnol. *13*, 730–738. https://doi.org/10.1038/s41565-018-0168-1.

16. Ludwanowski, S., Samanta, A., Loescher, S., Barner-Kowollik, C., and Walther, A. (2021). A Modular Fluorescent Probe for Viscosity and Polarity Sensing in DNA Hybrid Mesostructures. Adv. Sci. *8*, 2003740. https://doi.org/10.1002/advs.202003740.

17. Liu, W., Samanta, A., Deng, J., Akintayo, C.O., and Walther, A. (2022). Mechanistic Insights into the Phase Separation Behavior and Pathway-Directed Information Exchange in All-DNA Droplets. Angew Chem *134*, 202208951. https://doi.org/10.1002/ange.202208951.

18. Patel, A., Lee, H.O., Jawerth, L., Maharana, S., Jahnel, M., Hein, M.Y., Stoynov, S., Mahamid, J., Saha, S., Franzmann, T.M., et al. (2015). A Liquid-to-Solid Phase Transition of the ALS Protein FUS Accelerated by Disease Mutation. Cell *162*, 1066–1077. https://doi.org/10.1016/j.cell.2015.07.047.

19. Wang, J., Choi, J.-M., Holehouse, A.S., Lee, H.O., Zhang, X., Jahnel, M., Maharana, S., Lemaitre, R., Pozniakovsky, A., Drechsel, D., et al. (2018). A Molecular Grammar Governing the Driving Forces for Phase Separation of Prion-like RNA Binding Proteins. Cell *174*, 688-699.e16. https://doi.org/10.1016/j.cell.2018.06.006.

20. Loughlin, F.E., Lukavsky, P.J., Kazeeva, T., Reber, S., Hock, E.-M., Colombo, M., Schroetter, C.V., Pauli, P., Cléry, A., Mühlemann, O., et al. (2019). The Solution Structure of FUS Bound to RNA Reveals a Bipartite Mode of RNA Recognition with Both Sequence and Shape Specificity. Mol. Cell *73*, 490-504.e6. https://doi.org/10.1016/j.molcel.2018.11.012.

21. Ganser, L.R., Niaki, A.G., Yuan, X., Huang, E., Deng, D., Djaja, N.A., Ge, Y., Craig, A., Langlois, O., and Myong, S. (2024). The Roles of FUS-RNA Binding Domain and Low Complexity Domain in RNA-Dependent Phase Separation. Struct. Lond. Engl. 1993 *32*, 177-187.e5. https://doi.org/10.1016/j.str.2023.11.006.

22. Samanta, A., Sabatino, V., Ward, T.R., and Walther, A. (2020). Functional and Morphological Adaptation in DNA Protocells Via Signal Processing Prompted by Artificial Metalloenzymes. Nat. Nanotechnol. *15*, 914–921. https://doi.org/10.1038/s41565-020-0761-y.

467 23. Samanta, A., Hörner, M., Liu, W., Weber, W., and Walther, A. (2022). Signal-Processing and Adaptive Prototissue
468 Formation in Metabolic DNA Protocells. Nat. Commun. *13*, 3968. https://doi.org/10.1038/s41467-022-31632-6.

469 24. Liu, W., Lupfer, C., Samanta, A., Sarkar, A., and Walther, A. (2023). Switchable Hydrophobic Pockets in DNA Protocells
470 Enhance Chemical Conversion. J. Am. Chem. Soc. *145*, 7090–7094. https://doi.org/10.1021/jacs.3c00997.

471 25. Jutzi, D., Campagne, S., Schmidt, R., Reber, S., Mechtersheimer, J., Gypas, F., Schweingruber, C., Colombo, M., von
472 Schroetter, C., Loughlin, F.E., et al. (2020). Aberrant Interaction of FUS with the U1 snRNA Provides a Molecular
473 Mechanism of FUS Induced Amyotrophic Lateral Sclerosis. Nat. Commun. *11*, 6341. https://doi.org/10.1038/s41467-020-
474 20191-3.

475 26. Deng, H., Gao, K., and Jankovic, J. (2014). The Role of FUS Gene Variants in Neurodegenerative Diseases. Nat. Rev.
476 Neurol. *10*, 337–348. https://doi.org/10.1038/nrneurol.2014.78.

477 27. Ratti, A., and Buratti, E. (2016). Physiological Functions and Pathobiology of TDP-43 and FUS/TLS Proteins. J.
478 Neurochem. *138 Suppl 1*, 95–111. https://doi.org/10.1111/jnc.13625.

479 28. Dormann, D., and Haass, C. (2013). Fused in Sarcoma (FUS): An Oncogene Goes Awry in Neurodegeneration. Mol. Cell.
480 Neurosci. *56*, 475–486. https://doi.org/10.1016/j.mcn.2013.03.006.

481 29. Kamelgarn, M., Chen, J., Kuang, L., Jin, H., Kasarskis, E.J., and Zhu, H. (2018). ALS Mutations of FUS Suppress Protein
482 Translation and Disrupt the Regulation of Nonsense-Mediated Decay. Proc. Natl. Acad. Sci. U. S. A. *115*, E11904–
483 E11913. https://doi.org/10.1073/pnas.1810413115.

484 30. Dormann, D., Rodde, R., Edbauer, D., Bentmann, E., Fischer, I., Hruscha, A., Than, M.E., Mackenzie, I.R.A., Capell, A.,
485 Schmid, B., et al. (2010). ALS-Associated Fused in Sarcoma (FUS) Mutations Disrupt Transportin-Mediated Nuclear
486 Import. EMBO J. *29*, 2841–2857. https://doi.org/10.1038/emboj.2010.143.

487 31. Dormann, D., Madl, T., Valori, C.F., Bentmann, E., Tahirovic, S., Abou-Ajram, C., Kremmer, E., Ansorge, O., Mackenzie,
488 I.R.A., Neumann, M., et al. (2012). Arginine Methylation next to the PY-NLS Modulates Transportin Binding and Nuclear
489 Import of FUS. EMBO J. *31*, 4258–4275. https://doi.org/10.1038/emboj.2012.261.

490 32. Brelstaff, J., Lashley, T., Holton, J.L., Lees, A.J., Rossor, M.N., Bandopadhyay, R., and Revesz, T. (2011). Transportin1:
491 A Marker of FTLD-FUS. Acta Neuropathol. (Berl.) *122*, 591–600. https://doi.org/10.1007/s00401-011-0863-6.

492 33. Emmanouilidis, L., Bartalucci, E., Kan, Y., Ijavi, M., Pérez, M.E., Afanasyev, P., Boehringer, D., Zehnder, J., Parekh,
493 S.H., Bonn, M., et al. (2024). A Solid Beta-Sheet Structure Is Formed at the Surface of FUS Droplets during Aging. Nat.
494 Chem. Biol. *20*, 1044–1052. https://doi.org/10.1038/s41589-024-01573-w.

495 34. Shen, Y., Chen, A., Wang, W., Shen, Y., Ruggeri, F.S., Aime, S., Wang, Z., Qamar, S., Espinosa, J.R., Garaizar, A., et al.
496 (2023). The Liquid-to-Solid Transition of FUS Is Promoted by the Condensate Surface. Proc. Natl. Acad. Sci. *120*,
497 e2301366120. https://doi.org/10.1073/pnas.2301366120.

498 35. He, C., Wu, C.Y., Li, W., and Xu, K. (2023). Multidimensional Super-Resolution Microscopy Unveils Nanoscale Surface
499 Aggregates in the Aging of FUS Condensates. J. Am. Chem. Soc. *145*, 24240–24248.
500 https://doi.org/10.1021/jacs.3c08674.

501 36. Knowles, T.P.J., Vendruscolo, M., and Dobson, C.M. (2014). The Amyloid State and Its Association with Protein
502 Misfolding Diseases. Nat. Rev. Mol. Cell Biol. *15*, 384–396. https://doi.org/10.1038/nrm3810.

503 37. Iadanza, M.G., Jackson, M.P., Hewitt, E.W., Ranson, N.A., and Radford, S.E. (2018). A New Era for Understanding
504 Amyloid Structures and Disease. Nat. Rev. Mol. Cell Biol. *19*, 755–773. https://doi.org/10.1038/s41580-018-0060-8.

505 38. Dobson, C.M., Knowles, T.P.J., and Vendruscolo, M. (2020). The Amyloid Phenomenon and Its Significance in Biology
506 and Medicine. Cold Spring Harb Perspect Biol *12*, 033878. https://doi.org/10.1101/cshperspect.a033878.

39. Flory, P.J. (1942). Thermodynamics of High Polymer Solutions. J. Chem. Phys. *10*, 51–61. https://doi.org/10.1063/1.1723621.

40. Huggins, M.L. (1942). Some Properties of Solutions of Long-chain Compounds. J. Phys. Chem. *46*, 151–158. https://doi.org/10.1021/j150415a018.

41. Tompa, H. (1949). Phase Relationships in Polymer Solutions. Trans. Faraday Soc. *45*, 1142–1152. https://doi.org/10.1039/TF9494501142.

42. Scott, R.L. (1949). The Thermodynamics of High Polymer Solutions. V. Phase Equilibria in the Ternary System: Polymer 1—Polymer 2—Solvent. J. Chem. Phys. *17*, 279–284. https://doi.org/10.1063/1.1747239.

43. Strohm, L., Hu, Z., Suk, Y., Rühmkorf, A., Sternburg, E., Gattringer, V., Riemenschneider, H., Berutti, R., Graf, E., Weishaupt, J.H., et al. (2022). Multi-Omics Profiling Identifies a Deregulated FUS-MAP1B Axis in ALS/FTD–Associated UBQLN2 Mutants. Life Sci. Alliance *5*. https://doi.org/10.26508/lsa.202101327.

44. Alberts, B., Johnson, A., Lewis, J., Raff, M., Roberts, K., and Walter, P. (2002). Molecular Biology of the Cell 4th ed. (Garland Science).

45. Tanaka, H. (2022). Viscoelastic Phase Separation in Biological Cells. Commun. Phys. *5*, 1–12. https://doi.org/10.1038/s42005-022-00947-7.

46. van Steensel, B., and Belmont, A.S. (2017). Lamina-Associated Domains: Links with Chromosome Architecture, Heterochromatin, and Gene Repression. Cell *169*, 780–791. https://doi.org/10.1016/j.cell.2017.04.022.

47. Falk, M., Feodorova, Y., Naumova, N., Imakaev, M., Lajoie, B.R., Leonhardt, H., Joffe, B., Dekker, J., Fudenberg, G., Solovei, I., et al. (2019). Heterochromatin drives compartmentalization of inverted and conventional nuclei. Nature *570*, 395–399. https://doi.org/10.1038/s41586-019-1275-3.

48. Merindol, R., Delechiave, G., Heinen, L., Catalani, L.H., and Walther, A. (2019). Modular Design of Programmable Mechanofluorescent DNA Hydrogels. Nat. Commun. *10*, 528. https://doi.org/10.1038/s41467-019-08428-2.

49. Yue, L., Wang, S., Wulf, V., and Willner, I. (2019). Stiffness-Switchable DNA-Based Constitutional Dynamic Network Hydrogels for Self-Healing and Matrix-Guided Controlled Chemical Processes. Nat. Commun. *10*, 4774. https://doi.org/10.1038/s41467-019-12697-2.

50. Monahan, Z., Ryan, V.H., Janke, A.M., Burke, K.A., Rhoads, S.N., Zerze, G.H., O'Meally, R., Dignon, G.L., Conicella, A.E., Zheng, W., et al. (2017). Phosphorylation of the FUS Low-Complexity Domain Disrupts Phase Separation, Aggregation, and Toxicity. EMBO J. *36*, 2951–2967. https://doi.org/10.15252/embj.201696394.

51. Qamar, S., Wang, G., Randle, S.J., Ruggeri, F.S., Varela, J.A., Lin, J.Q., Phillips, E.C., Miyashita, A., Williams, D., Ströhl, F., et al. (2018). FUS Phase Separation Is Modulated by a Molecular Chaperone and Methylation of Arginine Cation-π Interactions. Cell *173*, 720-734.e15. https://doi.org/10.1016/j.cell.2018.03.056.

52. Hofweber, M., Hutten, S., Bourgeois, B., Spreitzer, E., Niedner-Boblenz, A., Schifferer, M., Ruepp, M.-D., Simons, M., Niessing, D., Madl, T., et al. (2018). Phase Separation of FUS Is Suppressed by Its Nuclear Import Receptor and Arginine Methylation. Cell *173*, 706-719.e13. https://doi.org/10.1016/j.cell.2018.03.004.

53. Zhao, J.Z., Xia, J., and Brangwynne, C.P. (2024). Chromatin Compaction During Confined Cell Migration Induces and Reshapes Nuclear Condensates. Nat. Commun. *15*, 9964. https://doi.org/10.1038/s41467-024-54120-5.

54. Shin, Y., Chang, Y.-C., Lee, D.S.W., Berry, J., Sanders, D.W., Ronceray, P., Wingreen, N.S., Haataja, M., and Brangwynne, C.P. (2018). Liquid Nuclear Condensates Mechanically Sense and Restructure the Genome. Cell *175*, 1481-1491.e13. https://doi.org/10.1016/j.cell.2018.10.057.

55. Lee, D.S.W., Strom, A.R., and Brangwynne, C.P. (2022). The Mechanobiology of Nuclear Phase Separation. APL Bioeng. *6*, 021503. https://doi.org/10.1063/5.0083286.

548 56. Mitrea, D.M., Mittasch, M., Gomes, B.F., Klein, I.A., and Murcko, M.A. (2022). Modulating Biomolecular Condensates:
549 A Novel Approach to Drug Discovery. Nat. Rev. Drug Discov. *21*, 841–862. https://doi.org/10.1038/s41573-022-00505-
550 4.

551 57. Jeon, S., Jeon, Y., Lim, J.-Y., Kim, Y., Cha, B., and Kim, W. (2025). Emerging Regulatory Mechanisms and Functions of
552 Biomolecular Condensates: Implications for Therapeutic Targets. Signal Transduct. Target. Ther. *10*, 1–42.
553 https://doi.org/10.1038/s41392-024-02070-1.

554 58. Schindelin, J., Arganda-Carreras, I., Frise, E., Kaynig, V., Longair, M., Pietzsch, T., Preibisch, S., Rueden, C., Saalfeld,
555 S., Schmid, B., et al. (2012). Fiji: An Open-Source Platform for Biological-Image Analysis. Nat. Methods *9*, 676–682.
556 https://doi.org/10.1038/nmeth.2019.

557